

Cite this: DOI: 10.1039/c2an35249d

www.rsc.org/analyst

PAPER

# Characterization of microstructured fibre emitters: in pursuit of improved nano electrospray ionization performance†

Xinyun Wu, Richard D. Oleschuk and Natalie M. Cann\*

Received 21st February 2012, Accepted 31st May 2012

DOI: 10.1039/c2an35249d

Full-dimensional computational fluid dynamics (CFD) simulations are presented for nano electrospray ionization (ESI) with various emitter designs. Our CFD electrohydrodynamic simulations are based on the Taylor–Melcher leaky-dielectric model, and the volume of fluid technique for tracking the fast-changing liquid–gas interface. The numerical method is first validated for a conventional 20  $\mu\text{m}$  inner diameter capillary emitter. The impact of ESI voltage, flow rate, emitter tapering, surface hydrophobicity, and fluid conductivity on the nano-ESI behavior are thoroughly investigated and compared with experiments. Multi-electrospray is further simulated with 2-hole and 3-hole emitters with the latter having a linear or triangular hole arrangement. The simulations predict multi-electrospray behavior in good agreement with laboratory observations.

## 1. Introduction

As a soft ionization technique, electrospray ionization (ESI) has revolutionized mass spectrometry (MS) especially for the analysis of large biomolecules.<sup>1</sup> Over the past decade there has been a clear trend towards the nano-ESI regime, which involves the analysis of solutions at a flow rate less than 1000 nL min<sup>−1</sup>.<sup>2</sup> A significant increase in ionization efficiency and sensitivity is possible from nano-ESI-MS due to the small size of the droplets produced, at a low flow rate, and these droplets require fewer Coulomb fission and desolvation events to yield a gas phase ion.<sup>3</sup> Traditional electrospray emitters are single-channeled, either tapered or non-tapered, and fabricated with pulling or etching techniques.<sup>4–6</sup> However, clogging and throughput problems greatly limit their applicability<sup>7</sup> and spray characteristics often differ between ostensibly identical emitters.

Novel emitter designs that split the incoming fluid into multiple channels have generated great attention for their enhanced robustness, sensitivity and sample utilization.<sup>2</sup> Moreover there is an additional gain in spray current for multi-sprays.<sup>8,9</sup> Relative to a single-channel spray current ( $I_s$ ) generated

at the same overall flow rate, the total current for the  $n$ -channel multi-spray is:<sup>9</sup>

$$I_{\text{total}} = \sqrt{n}I_s \quad (1)$$

provided each channel in the multi-spray emitter is operating in the cone-jet mode, and spraying independent of the other channels.

During the past few years, several novel emitters have been designed to achieve multi-electrospray (MES) where the total current increases with the square root of the number of channels.<sup>9–13</sup> Recently in our lab, a series of multichannel polycarbonate fibers possessing 3, 6, 9, 12 holes were designed and fabricated based on microstructured fiber (MSF) technology.<sup>14</sup> All channels were arranged in a radial pattern to ensure a homogenous electrospray from each channel. The spray current for these emitters follows the square root law in eqn (1), indicating the success of these designs to achieve true MES. Future MES designs will likely emphasize emitters that provide greater hole density, but interference between channels will ultimately limit the density that can be achieved while still generating independent sprays. Simulations have the potential to identify experimental conditions and hole patterns that maximize hole density while producing a spray current that follows eqn (1).

Most previous work on developing novel emitters<sup>11,12,15–20</sup> has been based on experiments, but the final spray performance is a result of the interplay between surface and fluid properties, emitter design, flow characteristics, applied field, and field variations at the tip. Knowledge of the interplay between these factors would greatly assist the design process. Early theoretical studies<sup>21–24</sup> started from an assumed initial shape of the liquid cone-jet and a certain charge distribution, and could only describe the steady cone-jet mode. Numerical simulations, especially for the entire dynamic ESI process are more

Department of Chemistry, Queen's University, Kingston, Ontario, Canada K7L 3N6. E-mail: natalie.cann@chem.queensu.ca; Fax: +1-613-533-6669; Tel: +1-613-533-2651

† Electronic supplementary information (ESI) available: A series of figures showing the mesh applied for different ESI emitter models and the corresponding boundary conditions is provided. A schematic of the experimental electrospray setup is included. For a single-channel emitter, a figure showing the quantitative assessment of the steady state is provided along with snapshots illustrating the formation of the Taylor-cone and jet for the Cartesian mesh. A snapshot of electrospray for the two-hole emitter where the channels are well separated is provided. See DOI: 10.1039/c2an35249d

challenging: the hydrodynamic solution of the free surface problem (gas and transient cone–jet) is already difficult. This is further complicated when electrostatic effects are coupled to the fluid dynamics, *i.e.* the electrohydrodynamics (EHD) regime. Moreover, the dramatic transformation from a cone shape into a thin jet is a tough mathematical and numerical problem.<sup>25</sup> Recently, commercial codes such as *FLUENT*,<sup>26</sup> *FLOW-3D*<sup>27</sup> and *CFX 4.4*<sup>26</sup> are introducing functionality to represent the flow problem, with the flexibility to be customized and adapted for flow in the presence of a field. Zeng *et al.*,<sup>28</sup> for the first time, reported a successful simulation of a full-dimensional Taylor cone–jet by extending the function of *FLOW-3D*. Their model was based on the Melcher–Taylor leaky dielectric model<sup>29</sup> using the Volume of Fluid (VOF) method. Similar simulations were later performed by Lastow and Balachandran<sup>30</sup> who customized *CFX 4.4*. Recently, Sen *et al.*<sup>31</sup> proposed an emitter model containing a multi-plumed array of carbon nanofibers, each vertically grown around the capillary orifice from a relatively large single capillary aperture (55  $\mu\text{m}$ ). While using computational fluid dynamics (CFD) as a tool for modeling electrospray ionization is only beginning, the many benefits it offers make it a rather promising field.

ESI experiments and CFD simulations, using *FLOW-3D*, are reported in this article. Numerical simulations are used to test the effect of various emitter designs on nano-ESI performance. We focus on one, two and three-hole emitters. Different regimes of the nano-ESI process are visually demonstrated and the impact of emitter geometry, flow rate, ESI voltage and liquid properties on the ESI performance are thoroughly investigated. The simulation predictions are compared with our empirical results. To our knowledge, the channel sizes considered here are the smallest that have been examined by CFD simulations.

This paper is organized as follows. In Section 2, the fundamental theory for simulating nano-ESI is briefly outlined. Simulation and experimental details are discussed in Sections 3 and 4 respectively. Section 5 reports results for one, two, and three hole emitters with validation tests presented as well. The geometric effect for hole density and pattern are demonstrated. Brief conclusions are presented in Section 6.

## 2. Theory

The CFD solution of the electrohydrodynamic flow equations can be viewed as a balance between hydrodynamic and electrostatic forces. Within the simulations, no assumptions are made for the initial shape of the Taylor cone or the charge distribution along the liquid–gas interface. All the liquid deformations and the changes in charge distribution are due to the forces acting on the system.

### 2.1. Physical model

Our CFD computations for simulating ESI are based on the well-established leaky dielectric model (LDM) proposed by Taylor and Melcher.<sup>32</sup> The liquid is a dielectric that allows free charge to exist at the liquid–gas interface. A shear force on these interfacial charges will act as the main driving force that induces the jet formation. Scheme 1 is an illustration of the force balance within the LDM. At the interface, normal electric stress is balanced by surface tension while viscous flow counterbalances the tangential component of the electric field.

Details of the relevant electrohydrodynamic equations have been provided elsewhere.<sup>29</sup> Only a brief description is given here. The break-up of the jet into droplets, and the dynamics of droplet evaporation have been a subject of considerable research interest for many years.<sup>33–35</sup> Within the CFD regime, only bulk characteristics are present and therefore droplets do not form, although certain regions of space may contain a small but non-zero amount of fluid.

### 2.2. Governing equations for fluid flow

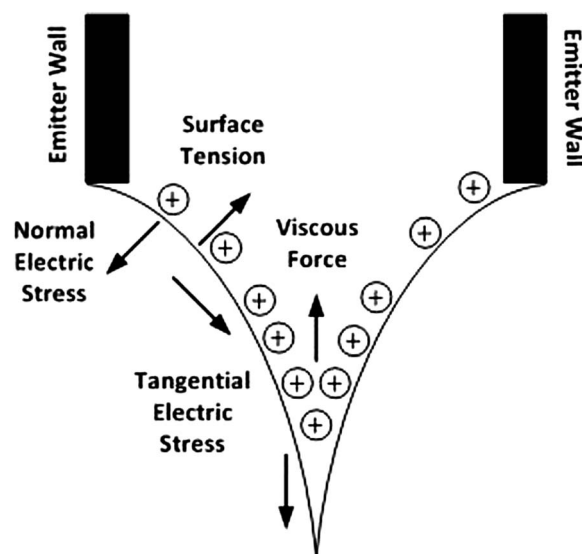
Three phases are involved in the simulations: the solid phase defines the emitter; the gas phase (air) acts as an insulator; and the liquid phase (spray solution) acts as a leaky dielectric. The simulation of flow is based on continuity relationships and conservation laws. Assuming the liquid to be incompressible (of constant density), Newtonian, with a constant viscosity and having laminar flow, the continuity of flow velocity can be expressed as

$$\nabla \cdot \vec{v} = 0 \quad (2)$$

where  $\vec{v}$  is the flow velocity, and  $\nabla \cdot$  is the divergence. Eqn (2) means that the local volume dilation rate is zero, which ensures continuous fluid flow. The modified Navier–Stokes equation for an EHD flow is,

$$\rho \frac{d\vec{v}}{dt} = -\nabla P + \eta \nabla^2 \vec{v} + \vec{f}_e + \rho \vec{g} \quad (3)$$

where  $P$  is the pressure,  $\vec{f}_e$  is the electromechanical force,  $\eta$  is the viscosity coefficient, and  $\vec{g}$  is the gravitational constant. The left side of the equation describes the acceleration of the fluid. The right side is the summation of several forces acting on the system: the first term is the force due to a pressure gradient  $\nabla P$ ; the second term describes the viscous force and, for incompressible flow, this is simply a shear effect; the fourth term is the force due to gravity; and the electromechanical force is discussed below.



**Scheme 1** Force distribution on the liquid cone–jet based on the leaky dielectric model.

The force arising from the applied field is captured by the electromechanical force,  $\vec{f}_e$ , given by:<sup>36</sup>

$$\vec{f}_e = q\vec{E} - \frac{1}{2}\vec{E} \cdot \vec{E} \nabla \epsilon \quad (4)$$

where  $\vec{E}$  is the electric field,  $\epsilon$  is the permittivity of the fluid, and  $q$  is the net free charge density near the interface. The first term on the right is the expected Coulomb force. The second term is due to polarization stress. Since the electric charges are located at the air–liquid interface, both the Coulomb force and polarization act at the interface.

### 2.3. Governing equations for the electric field

Along with the hydrodynamic equations presented above, the Laplace equation governing the LDM is introduced, with negligible bulk free charge density assumed, and the electric field is considered to be irrotational and divergence-free within the computational region. Thus the governing equation for the electric field in the bulk fluid region is:<sup>32</sup>

$$\nabla^2 \phi = 0 \quad (5)$$

where  $\phi$  is the electric potential. At the air–fluid interface, the charge conservation law is,

$$\frac{dq}{dt} = -\vec{n} \cdot \sigma(\nabla \phi) \quad (6)$$

where  $d/dt$  is the Lagrangian derivative, and  $\sigma$  is the electrical conductivity of the liquid. The vector  $\vec{n}$  represents the direction normal to the interface. The presence of the interfacial charge density then creates an electric field discontinuity in the direction normal to the interface while at the same time maintaining the conservation of current in the tangential direction. These two characteristics can be summarized as:

$$\vec{n} \cdot (\epsilon_l \nabla \phi_l - \epsilon_m \nabla \phi_m) = q \quad (7)$$

$$\vec{t} \cdot (\epsilon_l \nabla \phi_l - \epsilon_m \nabla \phi_m) = 0 \quad (8)$$

where  $\vec{n}$  is the unit normal to the surface,  $\vec{t}$  represents either of the two orthogonal tangent vectors embedded in the surface,  $q$  is the interfacial charge density, and  $\epsilon_l$  and  $\epsilon_m$  are the dielectric permittivity of the liquid and the medium, respectively.

### 2.4. The volume of fluid method and tracking of the air–liquid interface

In *FLOW-3D*, tracking of the moving air–fluid interface is achieved with the Volume of Fluid (VOF) technique, which was first developed by Hirt.<sup>37</sup> The basic idea is to introduce a fraction  $F$  for each cell.  $F$  represents the portion of the cell that is occupied by liquid:

$$F(x, y, z, t) = \begin{cases} 0 & \text{outside the liquid} \\ 1 & \text{inside the liquid} \\ > 0, < 1 & \text{on the free surface.} \end{cases} \quad (9)$$

To represent the dynamic nature of the interface,  $F$  fulfills the basic kinematic equation below:

$$\frac{dF}{dt} + \vec{v} \cdot \nabla F = 0 \quad (10)$$

where  $\vec{v}$  is the velocity of the fluid.

### 2.5. Spray current

At the base of the Taylor cone, charges are mainly transported by conduction to the liquid–air interface. The tangential electric stress at the interface then drives these charges toward the cone apex together with the surrounding liquid and causes convective flow. As a result, the current through the cone–jet has two contributions:<sup>23</sup>

$$I = I_{\text{cond}} + I_{\text{conv}} = \pi R_s^2 \vec{E}_z \sigma + 2\pi R_s \vec{u}_z q \quad (11)$$

where  $I_{\text{cond}}$  and  $I_{\text{conv}}$  are the conduction and convection currents, respectively,  $R_s$  is the jet radius,  $\vec{E}_z$  is the  $Z$ -component of the electric field on the surface of the jet,  $\vec{u}_z$  is the axial velocity of the jet and  $q$  is the surface charge density.

## 3. Simulation details

### 3.1. Simulation model

The solution for spraying is represented in our simulations with the following properties: density = 1030 kg m<sup>−3</sup>, viscosity = 0.008 Pa s, surface tension coefficient = 0.037 N m<sup>−1</sup>, dielectric constant = 55, electrical conductivity = 135 × 10<sup>−6</sup> S m<sup>−1</sup>. These parameters have been taken from ref. 38 and are chosen to represent a commonly used solvent for ESI: a 50% water, 50% methanol mixture that contains 1% acetic acid (v/v). This fluid definition is kept unchanged in all of our simulations, except for the single hole emitter where the conductivity was varied.

A constant velocity at the inlet of the emitter is defined to act like a pump that continuously drives the fluid through the channels. In all simulations, the channel is uniform with a 20 μm inner diameter. A high ESI voltage is applied to the emitter and a zero voltage plane is introduced to represent the counter electrode. The distance between the tip of the emitter and the zero voltage plane is 0.08–0.12 mm. This tip–plane separation is shorter than typical experimental distances but, within the simulations, this distance is long enough for the jet diameter and flow velocity to be well converged. A shorter tip–plane separation leads to a higher electric field in the simulations, when the applied voltage is comparable to experiment. Overall, to expedite the computations and to compensate for a higher field the flow rate in the simulations is also higher than in experiment.

Schematics of the emitter models examined in this work are provided in Fig. 1. Two single-aperture emitters are examined; one is externally tapered and the other has a flat tip. Two-hole emitter models are built with two identical channels being separated by 60 μm and 180 μm. Two three-hole emitter geometries have been modeled; the channels are either aligned or form an equilateral triangle. For the former, the channels are separated by 60 or 90 μm. The latter has channels separated by 180 μm.

The electrohydrodynamic equations discussed in Section 2 are solved with *FLOW-3D*. A numerical grid is applied and, as a result, a three-dimensional mesh is required to represent the

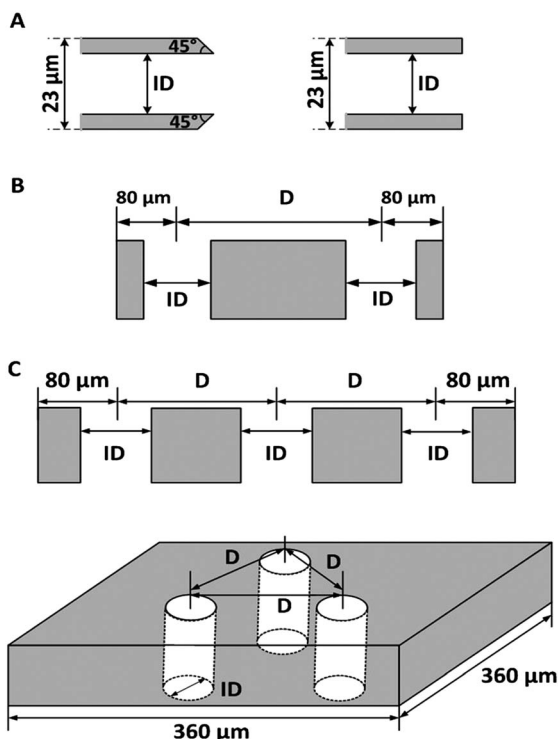


**Fig. 1** Illustration of simulated emitter models: (A) single-aperture emitter with externally tapered tip (left) or a flat tip (right); (B) two-aperture emitter with two channels being separated by  $D = 60 \mu\text{m}$  or  $D = 180 \mu\text{m}$ ; (C) three-aperture emitter with three aligned holes being equally separated by  $D = 60 \mu\text{m}$  or  $D = 90 \mu\text{m}$  (left). Three channels are positioned in a circular pattern with  $D = 180 \mu\text{m}$  (right).

simulation volume. If the mesh is too coarse, the simulations may crash or give unphysical results. On the other hand, a mesh that is too fine will greatly increase the computational time. For a single-aperture emitter, both Cartesian and cylindrical meshes can be applied but the latter is much more computationally efficient. The two and three hole emitters are best represented with a Cartesian mesh. We could, in principle, design a cylindrical mesh for these emitters but this would enforce symmetry between apertures and would produce a coarse grid in the region of the holes. Within the constraints of a Cartesian mesh, it is possible to embed a finer mesh within a coarser, overall mesh and this was implemented for the two and three-aperture emitters.

The meshes applied for the different ESI emitters are shown in Fig. S1†. In all cases, the apertures are aligned along the Z-direction. Both a cylindrical and a Cartesian mesh were chosen for the single-aperture emitter with the objective of gaining insight into an appropriate Cartesian mesh for the two- and three-aperture emitters. Fig. S1(A)† shows a slice through the R–Z plane for a uniform cylindrical mesh applied to the model for the single-aperture tapered emitter. Fig. S1(B)† shows the Cartesian mesh for the same emitter. Mesh sensitivity tests have been performed for both emitters, as discussed in Section 5.

Aside from the mesh sensitivity tests on single-aperture emitters, results are reported for a cylindrical mesh with 48 grid points in the radial direction (R). Within the aperture regions of each emitter, the Cartesian X–Y mesh is  $0.5 \mu\text{m} \times 0.5 \mu\text{m}$  to fully

characterize the cone and jet. A mesh of 100-to-120 points is applied in the Z-direction.

Fig. S1(C) and (D)† show the non-uniformity of the Cartesian mesh that is applied for the multi-hole models. The grid is uniform in the aperture region but varies non-uniformly elsewhere to limit the number of cells used for regions that are farther away from the cone-jets. Fig. S1(C)† shows the X–Z view of the Cartesian mesh applied for the two-aperture emitter. Only the upper half of the computational region is covered with mesh for calculations, with symmetry applied to generate the lower half. The aligned three-hole emitter model is similarly designed. An X–Y view for the triangular, three-hole model is shown in Fig. S1(D)†. In this case, no symmetry is applied to the computational region.

Boundary conditions are required to solve the electrohydrodynamic equations discussed in Section 2. Such conditions are required at the outer limits of the computational region and at the solid (emitter)–fluid interfaces. The characteristics of each boundary are shown in Fig. S2†. For all emitters, the fluid entering the computational region is represented with velocity boundary conditions (denoted by  $V$  in Fig. S2†) to guarantee a constant linear velocity of the fluid. This initial velocity does not directly correspond to the linear velocity within the actual channels since the computational region may not cover an entire hole and may begin with a fluid reservoir. At the other end, where fluid exits, continuative boundary conditions have been chosen. These conditions impose a constant velocity for Z beyond the computational region, thereby assuming that the fluid will neither accelerate nor decelerate after crossing the zero-voltage plane. A no-slip condition is applied to all emitter–fluid boundaries so that fluid in contact with the emitter wall has a zero velocity.

Additional boundary conditions are applied, depending on the type of mesh used and the characteristics of the computational region. For the single-aperture emitter represented by a cylindrical mesh, symmetric boundary conditions are introduced, and these act like a mirror with no flow or heat transfer across the boundary plane. In contrast, the same emitter represented with a Cartesian mesh requires two types of additional boundary conditions (Fig. S2(B)†): the two interior planes are set to be symmetric and the peripheral ones are outflow boundaries. The latter allows a constant acceleration of the liquid beyond the boundary plane, which is closer to the real physical condition. The boundary conditions for multi-hole ESI emitters are similar to the single-aperture Cartesian case with the interior planes being symmetric and the peripheral planes being outflow boundaries.

### 3.2. Spray current calculation

In order to calculate the spray current (eqn (11)), the jet radius, velocity, surface electric charge distribution, and the Z-component of the electric field along the jet surface need to be obtained. All of these physical quantities are probed at a Z value close to the zero-voltage plane. The first step is to locate the free surface region, where the liquid–gas boundary of the jet is located. Cells where the fraction of fluid is between 0 and 1 identify this region. The radius of the jet,  $r$ , at the specific Z value, is obtained by calculating



$$\pi r^2 = \frac{\sum_i F_i V_i}{\Delta Z} \quad (12)$$

where the sum runs over all cells fully or partially occupied by fluid,  $F_i$  is the fraction of fluid within the cell,  $V_i$  is the volume of the cell, and  $\Delta Z$  is the cell thickness. Fluid velocity in the  $Z$ -direction and the surface electric charge are regular outputs from the *FLOW-3D* simulation. The average fluid velocity is obtained by simply averaging the velocities reported for all fully or partially occupied cells at the specified  $Z$  value. The surface charge densities are generally highest for cells where  $F_i$  is small ( $<0.2$ ) but non-zero. We average over the cells at the outer limits of the jet to determine the surface charge density. Finally, the electric field magnitude at the surface of the jet is estimated by picking the two adjacent cells, above and below the chosen  $Z$  value. Then the electric potential for these cells is used to calculate a numerical derivative, which is the estimated  $Z$ -component of electric field at the surface.

### 3.3. Computational challenges for nano-ESI simulation

The simulation of nano-ESI processes is a rather challenging task. The ESI process itself is a complex interplay of many factors, thus the phenomenon is rather sensitive to any change in physical conditions both in experiment and in numerical simulations. Any change in hydrophobicity at the emitter tip surface, conductivity of solvent, *etc.* will affect ionization efficiency, spray stability, and spray current.

For the small amounts of fluid involved in a nano-ESI process, even small numerical errors during the simulation can lead to the collapse of the whole computation and thus should be strictly eliminated. The most common numerical error results from a charged mist appearing during the formation of the cone-jet. The existence of these mists greatly impacts the electric field uniformity and disturbs the computational stability. To improve the situation, we apply outflow boundaries for the peripheral computational region instead of the symmetric boundaries used by others.<sup>31,38</sup> In this way, the transient mists appearing within the computational region will exit the system once they reach the peripheral boundary. Also, the solid counter electrode plate was removed from the model and replaced by a zero voltage plane placed right at the boundary. This prevents the possibility of liquid collision with the endplate which can create backflow or droplets that disrupt the computational stability.

Besides the boundary setup, the controllable numerical parameters like mesh quality and computational time step are equally crucial to the success of simulation. Several measures are found to be useful in our experience. First, the mesh across the free surface needs to be as uniform as possible without causing convergence problems. Second, a mesh resolution finer than  $5 \times 10^{-7}$  m (cell size) should be used in and above the channels, otherwise, no jet will be produced. Third, the computational time step has to be strictly limited to less than 3 nanoseconds instead of relying on an automatic time step adjustment, otherwise, the computation fails. Overall, we find that a 3D Cartesian mesh is much more computationally demanding and the resulting 3D equations are more challenging to converge.

## 4. ESI experiments

### 4.1. Chemicals and materials

Glacial acetic acid and methanol (HPLC grade) were purchased from Fisher Scientific (Ottawa, ON, Canada) and used without purification. De-ionized water was obtained from a Milli-Q filtration system (Bedford, MA, USA). Electrospray solvents were degassed and filtered prior to use. The spray solvent was composed of 50% water and 50% methanol with 1% acidic acid (v/v) added as an ion source.

### 4.2. Specification and preparation of emitters

A single-nozzle TaperTip™ capillary was purchased from New Objective (Woburn, MA, USA, Catalogue no. TT360-20-50-N-5). The emitter is externally tapered leaving a uniform channel with a 20 μm inner diameter. This emitter design encourages cone formation, without increasing clogging in the tip region, to meet the rigorous demands of continuous electrospray.

ESI results for a three-channel MSF have recently been published.<sup>14</sup> In those experiments, a three-aperture polycarbonate MSF was designed in our lab and fabricated by Kiriam Pty Ltd (Sydney, Australia). The channels were placed at the apexes of an equilateral triangle to ensure every Taylor cone-jet experiences roughly the same electric field. Each channel had a 8–9 μm diameter, was 100 μm from the fiber edge, and the channel-to-channel separation was 402 μm. The large distance between the holes was chosen to ensure the generation of independent MES.

### 4.3. Electrospray for spray current measurement

A schematic of a typical electrospray setup for measuring the spray current is provided in Fig. S3†. The fluid was delivered to the emitter from a nano-flow gradient pump kindly provided by IDEX Health & Science LLC (Oak Harbor, WA, USA). A micro-tee is used to connect the emitter to the pump. A platinum wire is inserted into the third port of the micro-tee and a positive voltage is applied by a TriSep 2100 high-voltage module (Unimicro Technologies, Pleasanton, CA, USA). The counter electrode plate was held at ground and placed a short distance away from the emitter tip. A Keithley Picoammeter connected to the counter electrode plate is used to monitor the spray current where averaged signals were taken every 300 ms. Fig. S3† shows the experimental layout. The microscope is a Nikon Eclipse Ti-S (Nikon Canada, Mississauga, ON, Canada) and images and video were captured with a Nikon DS digital camera.

## 5. Results

This section begins with a detailed characterization of the single-aperture emitter. The results of mesh sensitivity tests are reported in Section 5.1. The impact of ESI voltage, flow rate, tapering at the tip, hydrophobicity, and fluid conductivity are examined in Section 5.2. Two- and three-aperture emitters are discussed in Sections 5.3 and 5.4, respectively. Calculated spray currents are discussed in Section 5.5.

### 5.1. Mesh sensitivity tests: single-channel emitters

The successful generation of a Taylor-cone and jet is shown in Fig. 2(A) together with iso-potential lines indicating the change of the electric field. By 0.08 milliseconds, a jet has formed with the base of the Taylor cone well confined by the tapered emitter tip. The corresponding electric field intensity contours are presented in Fig. 2(B) where the color variation identifies a large jump in the electric field across the free surface of the cone-jet. This electric field is responsible for the normal and tangential electric stresses; the normal stress maintains the cone shape while the tangential stress accelerates the liquid towards the jet.

Fig. S4(A)† shows the evolution of the mean kinetic energy of the fluid during the simulation. The kinetic energy dramatically increases as the Taylor cone-jet is generated and the fluid accelerates towards the zero-voltage plane. The evolution towards a steady state can also be monitored by examining the properties of a specific cell with time. For a Z-value on the jet surface, close to the zero-voltage plane, the time dependence of the potential, charge density, electric field magnitude, and velocity along the jet are provided in Fig. S4(B)–(E)†. All these parameters show that the computation approaches a steady state after roughly 0.0015 s when the fluctuations are less than 5%.

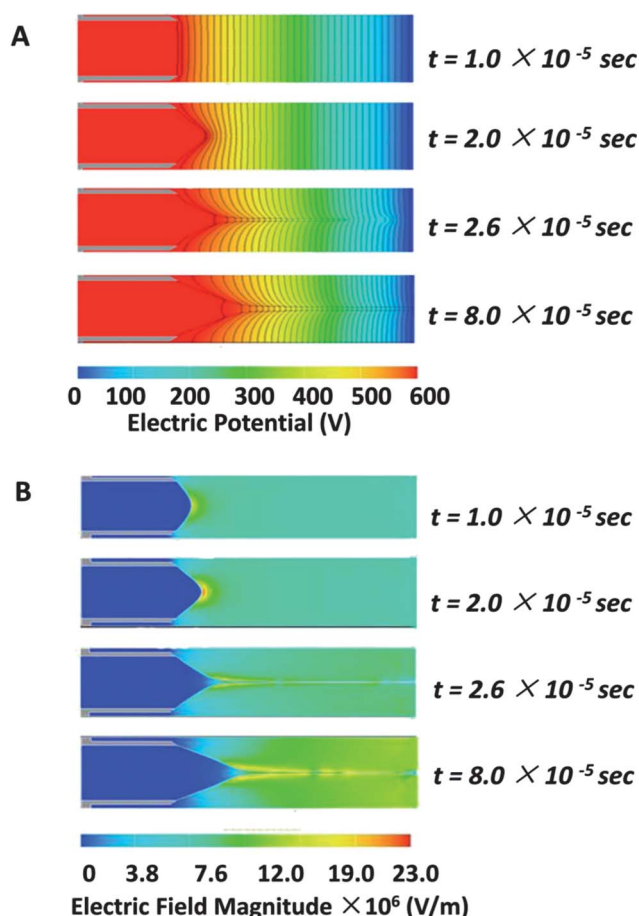


**Fig. 2** Simulation of Taylor-cone and jet formation for the single-aperture tapered emitter at a flow rate of  $0.06 \text{ m s}^{-1}$  and a voltage of 600 V. A cylindrical mesh is employed with a mesh size of  $5 \times 10^{-7} \text{ m}$ . Isopotential lines (A) and corresponding electric fields (B) are shown at different times.

The results of the cylindrical mesh convergence study are shown in Fig. 3(A). The jet is small and difficult to represent with a finite grid. For this reason, the jet radius serves as our measure of mesh convergence. We find that the jet radius is well converged for a cell size of  $2.5 \times 10^{-7} \text{ m}$  or smaller. A comparison between the CPU time for a single time step (1 microsecond), the cell size, and the total number of cells is shown in Fig. 3(B). As expected, a finer grid increases the computational time. Taking into consideration both the accuracy and the efficiency of the computation, a mesh size of  $2.5 \times 10^{-7} \text{ m}$  was chosen.

As a preparation for multi-nozzle electrospray emitters, where a cylindrical mesh is no longer practical, a Cartesian mesh sensitivity test was performed on the same model. With the change in computational region, from 2D cylindrical to 3D Cartesian, the number of cells has increased significantly (see Table 1). As a result, the CPU time for a simulation that uses a Cartesian mesh is considerably longer. As an illustration, a successful generation of a 3D electrospray within the computational region is shown in Fig. S5†. The electric charge density contours show that charge accumulates on the liquid surface, as expected, and is gradually transported towards the counter electrode.

The results from the Cartesian mesh convergence test are shown in Fig. 3(C) and (D). The jet radius and CPU time, as a function of the mesh, show that the optimal mesh size is around  $2.5 \times 10^{-7} \text{ m}$ . This mesh is a good compromise between accuracy and computational efficiency. This value will be used in the aperture regions of the two-hole and three-hole emitters.

### 5.2. Characterization of nano-ESI: single-channel emitters

In ESI experiments, the characterization curve that relates spray current to the ESI voltage is often used to identify the spraying mode and, in particular, the operationally stable cone-jet mode. Smith *et al.* suggest that the morphology of the Taylor cone should also be considered when determining the stability island of the cone-jet mode.<sup>39</sup>

Electrospray simulations were conducted for a broad range of applied voltages and flow rates to identify the stable cone-jet region. Operational parameters that are able to generate the cone-jet in the simulations are indicated by the shaded region of Fig. 4. However, this region also includes some unstable states where the cone is either too small or too elongated to be consistent with the shape Taylor predicted, and the jet keeps growing and shrinking with a certain frequency. A conclusive determination of the stable cone-jet mode requires also the investigation of the spray current.

Fig. 5(A) shows a typical characterization curve from the simulations at a constant inflow velocity of  $0.04 \text{ m s}^{-1}$ . With an increasing electric field, several regimes of electrospray are obtained. At low fields, a dripping mode is observed since there is not enough force to transport the fluid away and the cone adopts a round shape and deforms towards the counter electrode. Droplets or jets burst out periodically to decrease the surface energy of the growing cone. Every 'burst-out' event results in the cone returning to its original shape and then the process repeats (Fig. 6(A)). As the voltage increases, the droplet gradually decreases in size and, eventually, a pulsating regime is observed where the Taylor cone grows and shrinks. A further increase in

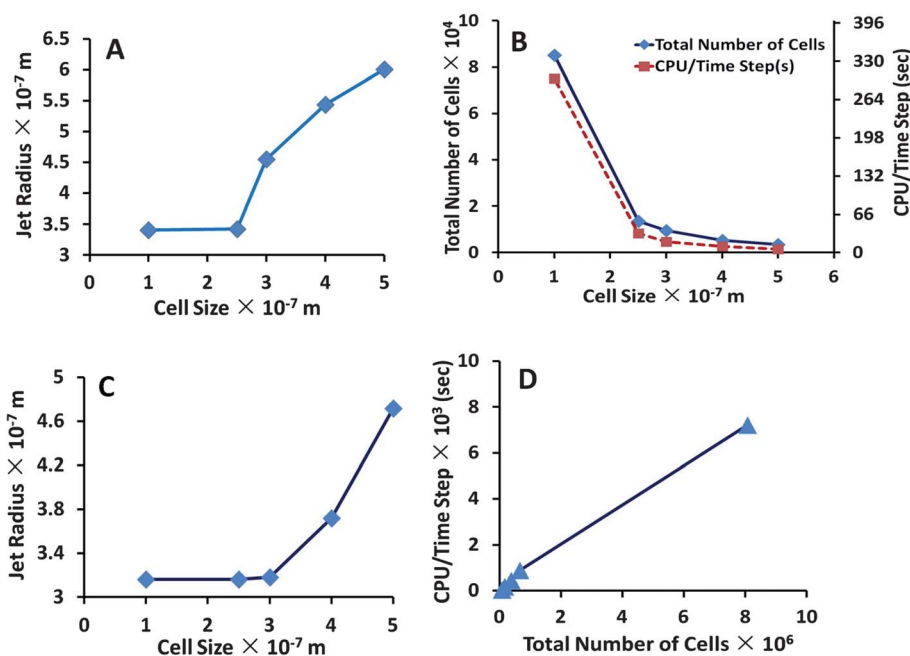


**Fig. 3** (A) Average jet radius at the zero-voltage plane, plotted as a function of the cell; (B) relationship between total number of cells (blue line), CPU time for the first time step (red line), and the computational cell size of the 2D cylindrical mesh; (C) averaged jet radius at the zero-voltage plane, plotted versus mesh resolution for the 3D Cartesian mesh; (D) CPU time required for the first time step ( $1 \times 10^{-6}$  s) versus corresponding total number of cells.

**Table 1** Comparison of the number of cells, under the same mesh resolution, for cylindrical and Cartesian meshes

Cell size $\times 10^{-7}$ m	Total number of cells (cylindrical)	Total number of cells (Cartesian)
5	3408	81 792
4	5340	160 200
3	9480	379 200
2.5	13 632	654 336
1	85 200	8 064 000

voltage yields the cone-jet regime, where a pointed cone is formed with well-defined edges. Moreover, within this regime, the spray current appears to be independent of ESI voltage. When the voltage is too high, there is not enough support for the fluid, the jet is too thin and frequently breaks up, and stability is

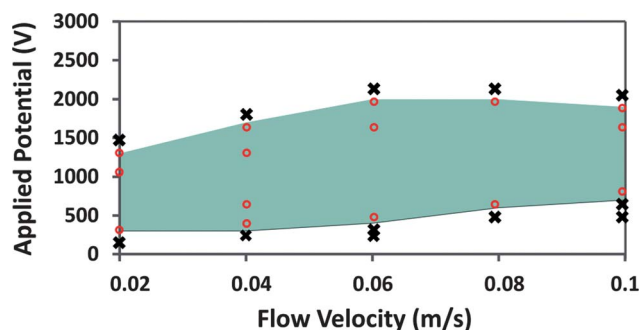


**Fig. 4** Simulation predictions of the operational cone-jet mode (shaded area) for the single-aperture tapered emitter. Circles represent the simulation trials that are successful in forming the cone-jet,  $\times$  represents the simulation trials that fail to form a cone-jet.

lost (Fig. 6(B)). All these simulation results are consistent with available literature<sup>40,41</sup> and our own experimental observations shown in Fig. 5(B).

Besides the ESI voltage, flow rate is another important operational parameter for ESI performance. By increasing the flow rate at a constant voltage of 1.5 kV, our experiments show that the Taylor cone grows in size (Fig. 7(A)). The simulations show the same tendency for the growth of the cone (Fig. 8(A)). Because of the small size of the jet and the limitations in the imaging equipment, the jet cannot be directly observed in our experiments. However, the jet can be observed in the simulations and we find that a thicker jet is produced with a larger cone (Fig. 7(B)). This result is consistent with the preference for low flow rates in ESI experiments, since a thinner jet yields smaller droplets.

Wetting of the emitter tip is a common problem in ESI experiments. A tapered emitter tip is often chosen to minimize wetting. To explore the connection between tapering and wetting, parallel simulations were performed under the same flow rate and field conditions with a flat-tip emitter and a tapered-tip emitter. When the contact angle is set to 30 degrees, the liquid wets to the outer periphery of the flat tip (Fig. 8(A)). Under even stronger wetting conditions, shown in Fig. 8(B), the liquid wets all over the emitter tip and no cone-jet can be supported. The situation is greatly improved with a tapered design under the same wetting conditions, where a stable cone-jet is generated and restricted to the inner wall of the channel (Fig. 8(C)).

In most ESI experiments, additives like acetic acid are often included in the spray solution to enhance conductivity, protonate silanol groups on the wall, and to provide a source of protons for ionizing analytes. The impact of the change in conductivity on spray performance is shown in Fig. 9. Simulations show that a thinner jet is generated by a more conductive solvent.

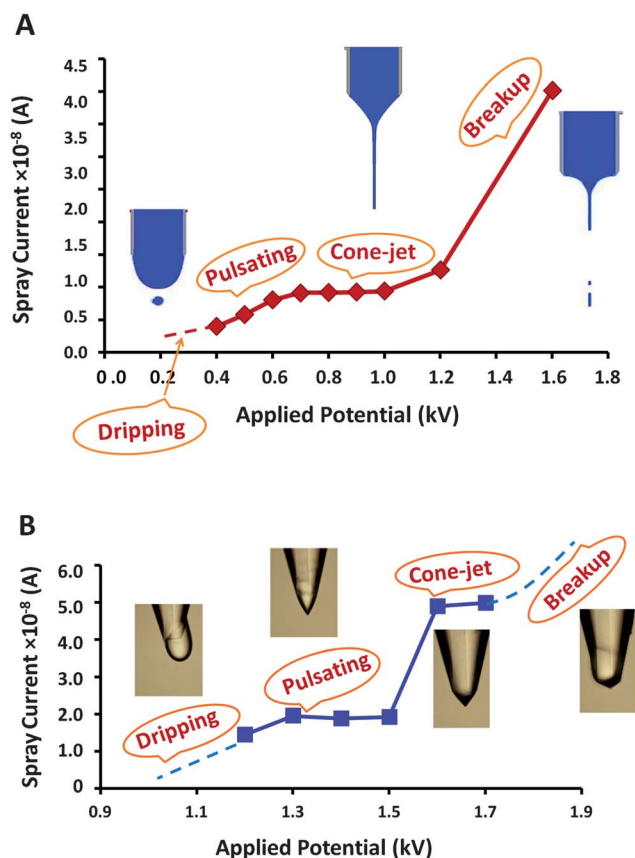


**Fig. 5** A comparison of simulated and measured nano-ESI characterization curves for single-aperture tapered emitters. (A) The relationship between spray current and ESI voltage for a  $20 \mu\text{m}$  inner diameter at a constant inflow velocity of  $0.04 \text{ m s}^{-1}$  (equals  $753.6 \text{ nL min}^{-1}$ ). (B) Experimental results measured at a constant inflow velocity of  $30 \text{ nL min}^{-1}$ .

Moreover, the surface electric charge distribution, which is the charge per surface area along the jet, increases significantly with enhanced conductivity. Fig. 9(A) illustrates that better ESI performance is obtained by spraying a more conductive solvent: a smaller initial droplet size with a higher electric charge density will be produced. As expected, the spray current increases (Fig. 9(B)) with a higher electric conductivity. These simulation predictions are in good agreement with previous studies.<sup>42,43</sup>

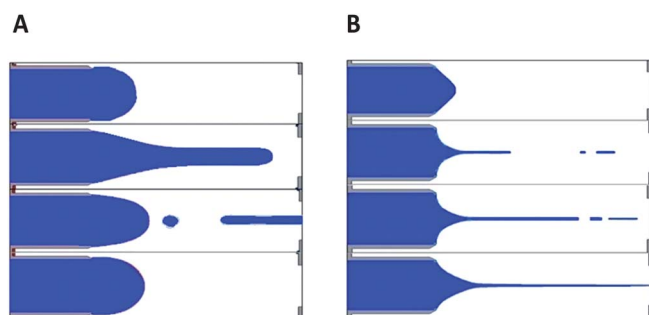


**Fig. 6** Simulated unstable regimes for the single-aperture tapered emitter. Snapshots are shown 0.22, 0.5, 0.56, and 0.6 milliseconds. (A) Dripping mode, where the voltage 100 V is used under the applied inflow rate of  $0.02 \text{ m s}^{-1}$ ; (B) Breakup mode, where a voltage of 1600 V is used with an inflow velocity of  $0.04 \text{ m s}^{-1}$ .

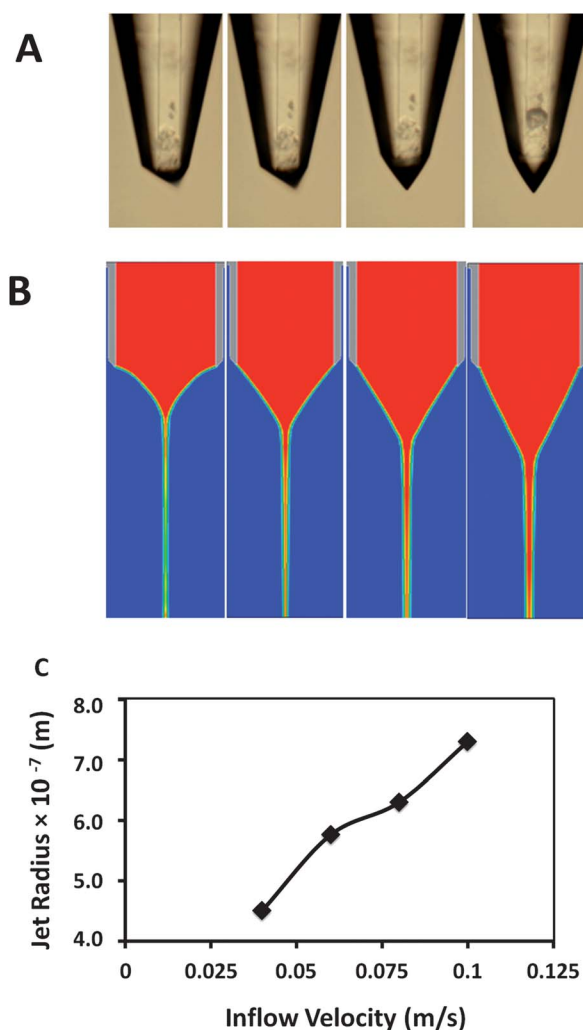


**Fig. 7** Variation of the Taylor cone and jet, at a constant ESI voltage of 1.5 kV and flow rates of 20, 30, 40, and  $50 \text{ nL min}^{-1}$ . The flow rate increases from left to right in the panels above. (A) Experimental Taylor-cones, (B) Taylor-cones and jets from simulations, and (C) simulation predictions for the change of jet radius with increasing inflow velocity.

### 5.3. Nano-ESI simulations with two-hole emitter

Two two-hole emitters have been considered, with center-to-center distances of  $60 \mu\text{m}$  and  $180 \mu\text{m}$ . The simulations have a fluid inflow velocity of  $0.09 \text{ m s}^{-1}$  and a voltage of 2000 V. The initial onset voltage is found to be several hundreds of volts higher than for the tapered-tip single-channel emitter under the same inflow velocity. This is due to the fact that the tapered shape induces a higher local electric field than a flat tip.

At smaller aperture separation, interactions between the jets are expected but, at  $180 \mu\text{m}$ , the distance is large enough to anticipate that the jets will be independent. The profiles of the two electrosprays are shown in Fig. S6† together with electric potential contours. Two Taylor-cones and jets are successfully generated and the two jets appear to be semi-parallel. In addition, the electric field lines between the channels are parallel to the emitter surface, indicating that the neighboring cone-jets have little impact on each other at this separation. We conclude



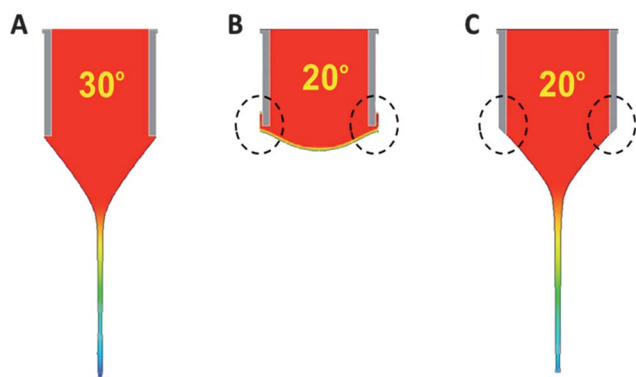


**Fig. 8** (A) Simulated electrospay under contact angle of 30 degrees with a flat-tip emitter; (B) simulated electrospay under contact angle of 20 degrees with a flat-tip emitter where no cone-jet formed; (C) simulated electrospay under contact angle of 20 degrees with a tapered emitter. All simulations are performed at an applied potential of 800 V and a flow rate of  $0.07 \text{ m s}^{-1}$ .

that a  $180 \text{ }\mu\text{m}$  separation is sufficient to yield emitters that are effectively independent.

To investigate the influence of the distance between holes on multi-electrospray performance, similar simulations were performed with the distance between the two holes reduced to only  $60 \text{ }\mu\text{m}$ . As expected, a strong repulsion between the two cone-jets occurs since they are closer together and both are positively charged on the surface of the jet. This leaves each jet experiencing an additional Coulomb force that acts to push the jets away from each other. Additional simulations were further performed (Fig. 10(A)–(C)) under varying ESI voltage, keeping all other physical parameters the same. With increased voltage, the jets

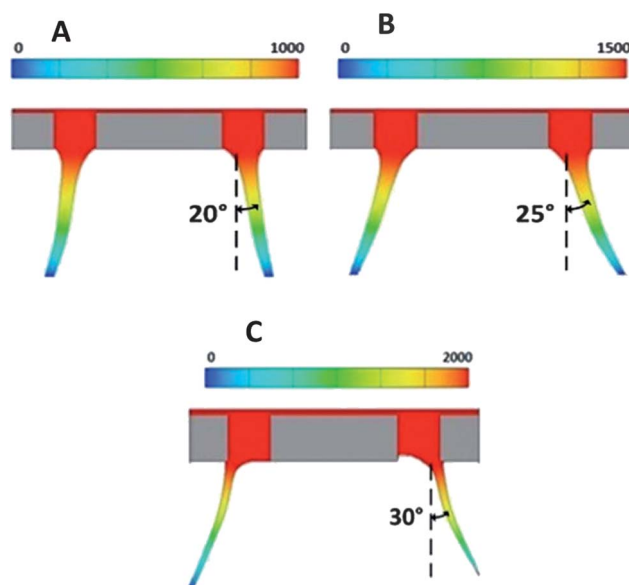


**Fig. 10** Effect of ESI voltage on multi-electrospray performance for the two-aperture emitter with the channels  $60 \text{ }\mu\text{m}$  apart. The inflow velocity is  $0.09 \text{ m s}^{-1}$  while the applied voltage of 1000 V (A), 1500 V (B), and 2000 V (C). The repulsion between the jets, measured by the angle between the jet and the aperture axis, increases with applied voltage.

become thinner, and the repulsion between them increases, as shown by the angle between the jet and the channel axis. When the voltage is 2000 V, the base of the Taylor cone moves outwards and is nearly beyond the channel. This is consistent with multispray experiments<sup>14</sup> where repulsion moves the cones and jets away from the holes.

Fig. S6† and 10 show instantaneous snapshots during the electrospay process for different channel separations and ESI voltages. Note that the jets are not identical in the snapshots. Instantaneous differences in the jets ultimately begin from small discrepancies in the channel dimensions and in the channel placement within the overall emitter grid (see Fig. S1†). Over time, these minor differences lead to cones and jets that are different too. If sufficiently long computations are run, average properties will be indistinguishable for both channels. We could impose symmetry constraints to suppress dynamical fluctuations but these fluctuations duplicate the experimental situation where field non-uniformity, emitter imperfections, and other factors, lead to cones and jets that are not identical. In fact, symmetry constraints would reduce the computing time but our emitter models have been chosen to ensure that dynamical fluctuations can occur.

#### 5.4. Nano-ESI simulation with three-hole emitter

Arrays of ESI emitters have been reported as a way to enhance the ionization efficiency.<sup>9,14,16,17,44</sup> However, closely spaced emitter arrays introduce a deleterious shielding effect from neighboring channels. To be precise, the channels experience different local fields and may operate in different spray regimes. Thus shielding limits the range of flow rate and voltage where all channels form a cone jet. Though the exact mechanism for this

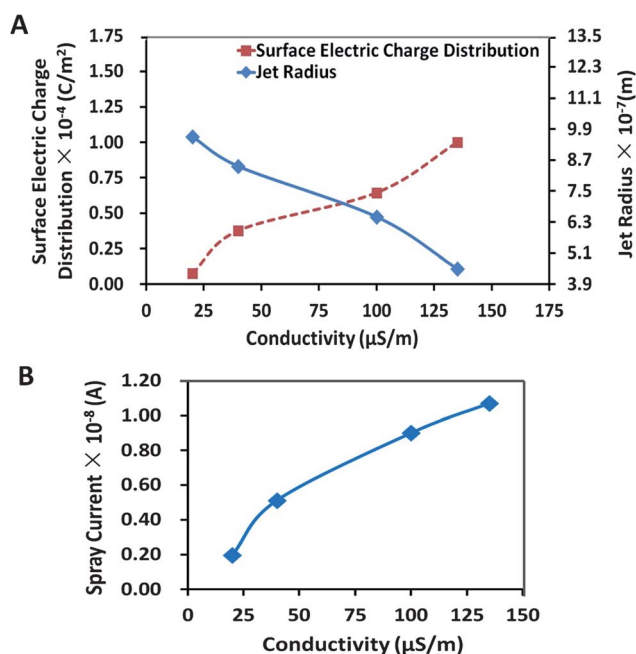


**Fig. 9** The impact of varying conductivity for the single-aperture tapered emitter, at a voltage of 800 V and a constant inflow velocity of  $0.09 \text{ m s}^{-1}$ ; (A) the jet radius (dash line) and surface electric charge distribution (solid line); (B) the connection between spray current and conductivity.

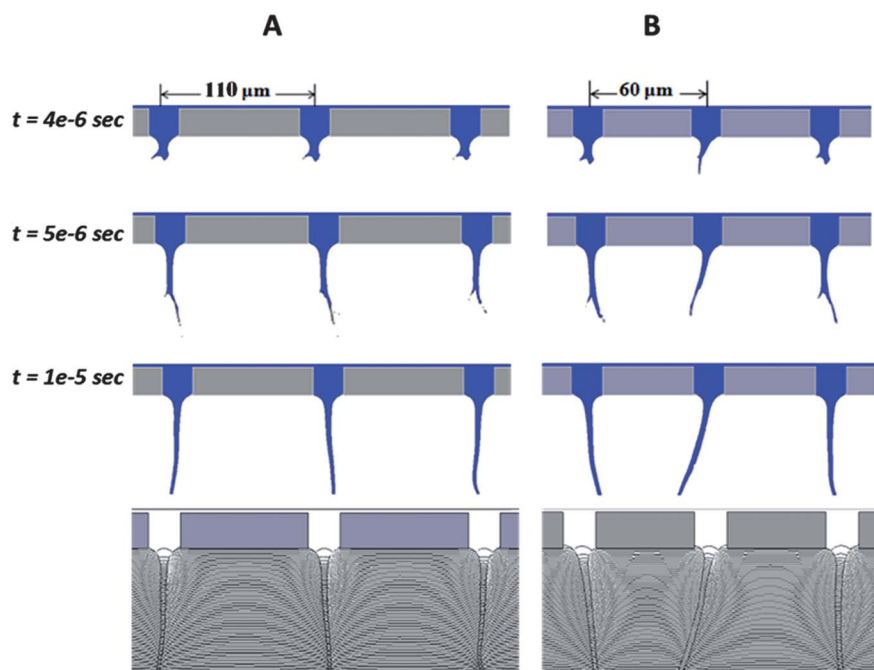


**Fig. 11** Snapshots of the simulated multi-sprays for the linear three-channel emitter arrays at an applied voltage of 2 kV and an inflow velocity of  $0.02 \text{ m s}^{-1}$ . The apertures are separated by  $110 \mu\text{m}$  (A) and  $60 \mu\text{m}$  (B). The last row shows the electric field lines at  $1 \times 10^{-5} \text{ s}$ .

shielding effect is not yet clear, the space charge created from jet breakup is found to be an important contributor.<sup>45</sup>

To investigate the shielding effect in the absence of the space charge contribution, ESI simulations with aligned three-hole emitters were performed with two channel separations:  $110 \mu\text{m}$

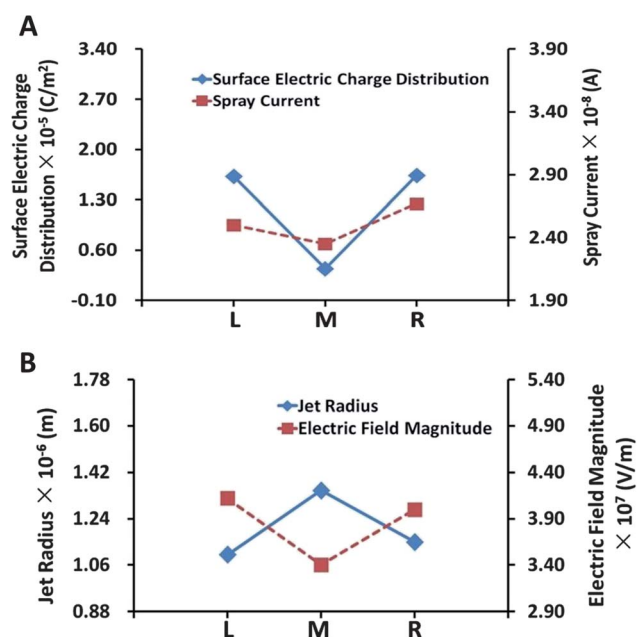


**Fig. 12** Comparisons of the jet properties for the three-aperture emitter in Fig. 11. The labels L, M and R refer to the left, the middle and the right jets respectively. (A) Difference of jet radius and electric field magnitude between the three aligned jets. (B) Difference of surface electric charge distribution and spray current for the three aligned jets.

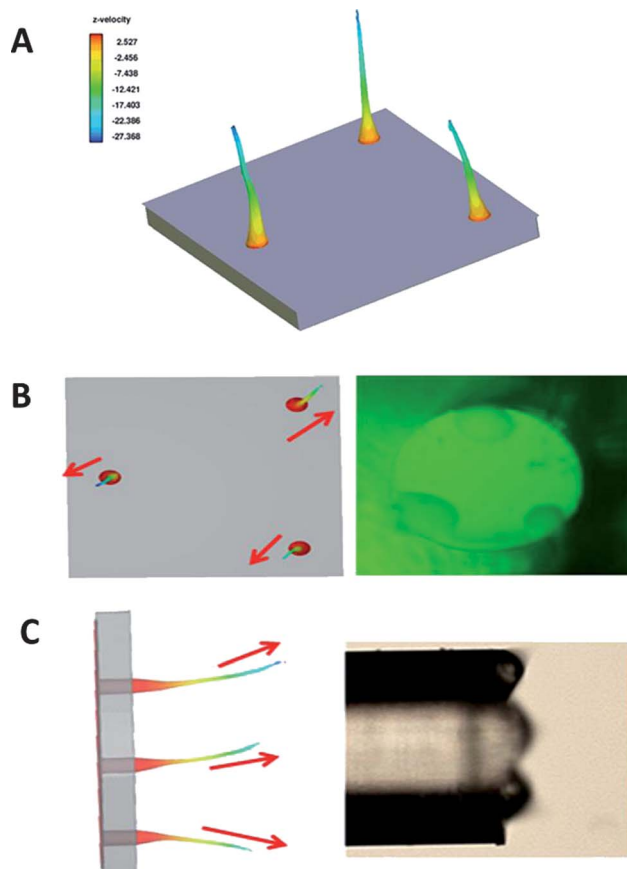


**Fig. 13** (A) 3D view of the simulated multi-ESI for the triangular 3-hole emitter under inflow velocity of  $0.02 \text{ m s}^{-1}$  and applied voltage of 2 kV. Comparison of multiple electro spray with 3-aperture emitter<sup>4</sup> showing similar repulsion between charged jets on  $X$ - $Y$  (B) and on  $Y$ - $Z$  planes (C) respectively.

**Table 2** Spray current from a one-hole, two-hole, and a linear three-hole emitter. The one-hole model is a flat tip emitter. The hole spacing, distance between the emitter and the zero-voltage plane, ESI voltage, and linear flow velocity are given to fully characterize the emitter. The spray current is calculated as discussed in Section 3.2. The final column shows the calculated constant  $C$  from eqn (13)

	Hole spacing	Spray distance	ESI voltage (V)	Velocity <sup>a</sup> (m s <sup>-1</sup> )	Total flow rate <sup>a</sup> $Q$ (m <sup>3</sup> s <sup>-1</sup> )	Total spray current $I$ (A)	$C$ (A [s m <sup>-3</sup> ] <sup>1/2</sup> )
1-hole	N/A	0.07 mm	2000	0.09	$9.42 \times 10^{-11}$	$2.98 \times 10^{-8}$	$3.1 \times 10^{-3}$
2-hole	60 $\mu$ m	0.07 mm	2000	0.06	$1.20 \times 10^{-9}$	$1.40 \times 10^{-7}$	$2.9 \times 10^{-3}$
2-hole	180 $\mu$ m	0.07 mm	2000	0.04	$1.20 \times 10^{-9}$	$1.51 \times 10^{-7}$	$3.1 \times 10^{-3}$
3-hole	60 $\mu$ m	0.07 mm	2000	0.04	$4.80 \times 10^{-10}$	$7.59 \times 10^{-8}$	$2.0 \times 10^{-3}$
3-hole	90 $\mu$ m	0.07 mm	2000	0.04	$4.80 \times 10^{-10}$	$9.30 \times 10^{-8}$	$2.5 \times 10^{-3}$

<sup>a</sup> The linear flow velocity refers to flow into the computational zone, which may include a reservoir. This zone may differ for the various emitters. The flow rate, in m<sup>3</sup> s<sup>-1</sup>, is calculated from the linear flow velocity and the size and shape of the computational zone, including the impact of a reservoir if present.

and 60  $\mu$ m. Simulations were performed under the same applied voltage of 2 kV and the same inflow velocity of 0.09 m s<sup>-1</sup>. Fig. 11 shows the multi-spray behavior during cone-jet formation at different times for both channel separations. When the channels are well-separated, the three cone-jets remain similar from the very beginning to the end (Fig. 11(A)) of the simulation with hardly any interference observed.

When the three channels are aligned and 60  $\mu$ m apart, the electrospray generated from the interior emitter differs from the other two. The field lines at 0.05 milliseconds are provided in Fig. 11 and show a much more complicated pattern, with clear interaction between neighbouring channels. A detailed investigation of the three jets was performed close to the zero-voltage plane, to quantify the differences. As shown in Fig. 12(B), the middle jet experiences the lowest electric field, while the other two are roughly the same. Moreover a slightly thicker jet is produced in the middle due to the weaker electric field. Differences in surface electric charge distribution and the spray current are shown in Fig. 12(A). The two peripheral jets have similar properties but their spray current is significantly higher than for the middle jet. With both a thicker jet produced and at a lower charge density as well as spray current, the operational regime in the middle jet is less favorable compared with the outer emitters.

To balance the electric shielding effect across the channels of a multi-electrospray system, a circular pattern<sup>15</sup> of channels has been proposed. Using a similar idea, a simulation was performed for a three-hole emitter with channels being positioned at the apexes of an equilateral triangle. The successful generation of multi-electrospray is presented in Fig. 13(A). Though three cone-jets have formed, the interference among the jets is clearly seen. Qualitative comparisons with the experimental observation from different views are shown in Fig. 13(B). Instead of pointing straight toward the zero-voltage plane, the three jets repel one another. The phenomenon is rather similar to the experiments shown on the right.

### 5.5. Calculated spray currents

The basis for the expected current increase of a multi-electrospray system, summarized in eqn (1), is a relationship between current,  $I$ , and flow rate,  $Q$ , proposed by de la Mora and Loscertales.<sup>42</sup> Generalizing to a multi-spray system, this relationship is

$$I = \sqrt{n} f(\varepsilon) \left[ \frac{Q K \gamma}{\varepsilon} \right]^{\frac{1}{2}} = C \sqrt{n} Q^{1/2} \quad (13)$$

where  $n$  is the number of independent channels,  $K$  is the conductivity,  $\gamma$  is the surface tension, and  $\varepsilon$  is the dielectric constant of the liquid. We have examined this relationship for the one, two, and linear three-hole emitters and the results are summarized in Table 2. The channels are separated by 60–180  $\mu$ m. The ESI voltage is kept constant along with all the fluid properties in the simulations. Under these conditions the same value for  $C$  is expected if the channels are operating independently. That is, the  $\sqrt{n}$  scaling shown in eqn (1) will occur only if a constant  $C$  value is calculated for the one-, two-, and three-hole emitters. If multispray performance is reduced for the multichannel emitters, then the corresponding spray current will be reduced along with the calculated value for  $C$ .

From the simulations, we calculate that  $C$  is roughly 0.003 A (s m<sup>-3</sup>)<sup>1/2</sup> for the one-channel emitter. A very similar value is obtained from the two-channel emitter for both channel separations, with only a slight reduction when the channels are closer. For the three-channel emitter,  $C$  is calculated to be much smaller when the apertures are separated by only 60  $\mu$ m. This indicates that shielding, in the linear three-channel emitter, has led to a reduced current as expected from Fig. 11 and 12.

A more detailed, quantitative analysis of the shielding would require a better estimate of the spray current. For this, a finer grid, applied over a greater region of the computational region, would be required since the jet radius, fluid velocity in the  $Z$ -direction, surface charge density, surface electric charge, and electric field magnitude at the surface of the jet are all required to calculate the current (eqn (13)) but all are impacted by the grid.

## 6. Conclusion

CFD has been successfully applied to the simulation of the dynamic process of nano-ESI and the methodology has proved to be rather effective at testing the geometric effect of the ESI emitter. Simulation predictions for single-channel nano-ESI behavior under various operational regimes show good agreement with previous literature<sup>40</sup> and our experiments.

Multi-electrospray was successfully simulated with two-hole and three-hole emitter models. The impact of hole-spacing was investigated and relatively independent cone-jets are formed when the distance between the holes is large. A significant

repulsion between the charged jets is observed when the holes are closer to each other, conforming to experimental observation. The effect of ESI voltage was examined for the two-hole emitter and the results indicate a greater repulsive force under a higher electric field. Three-hole emitters were simulated with two different emitter designs. For an aligned emitter array, channel spacing is varied to test the electric shielding effect. Though space charges are not considered in our model, interference from neighboring sprays makes the interior emitter act differently due to the weaker electric field. For the model with a triangular pattern for the three channels, the repulsion among charged jets is significant even for a channel separation where the two-channel emitter indicated minimal channel-to-channel interactions. This result points to a many-body (many-jet) contribution to shielding.

Future simulations will focus on elucidating a detailed shielding mechanism, on exploring a wider range of emitter designs, and on improving the charge current calculations.

## Acknowledgements

Technical advice provided to X. Wu by A. Chandorkar, J. Huang, E. Su, and J. Ditter at *FLOW-3D* is gratefully acknowledged. The authors wish to thank G.T.T. Gibson for advice provided on nano-ESI experiments. The provision of a nano-flow gradient pump by IDEX Health & Science LLC (Oak Harbor, WA, USA) is gratefully acknowledged. The authors also wish to acknowledge Queen's University, CMC Microsystems, and the Natural Sciences and Engineering Research Council of Canada (NSERC) for funding.

## References

- 1 J. B. Fenn, M. Mann, C. K. Meng, S. F. Wong and C. M. Whitehouse, *Science*, 1989, **246**(4926), 64–71.
- 2 G. T. T. Gibson, S. M. Mugo and R. D. Oleschuk, *Mass Spectrom. Rev.*, 2009, **28**(6), 918–936.
- 3 P. Kebarle and U. H. Verkerk, *Mass Spectrom. Rev.*, 2009, **28**(6), 898–917.
- 4 M. Wilm and M. Mann, *Anal. Chem.*, 1996, **68**(1), 1–8.
- 5 D. R. Smith, G. Sagerman and T. D. Wood, *Rev. Sci. Instrum.*, 2003, **74**(10), 4474–4477.
- 6 S. Le Gac, C. Rolando and S. Arscott, *J. Am. Soc. Mass Spectrom.*, 2006, **17**(1), 75–80.
- 7 N. B. Cech and C. G. Enke, *Mass Spectrom. Rev.*, 2001, **20**(6), 362–387.
- 8 J. Fernández de la Mora and I. G. Loscertales, *J. Fluid Mech.*, 1994, **260**, 155–184.
- 9 K. Tang, Y. Lin, D. W. Matson, T. Kim and R. D. Smith, *Anal. Chem.*, 2001, **73**(8), 1658–1663.
- 10 Q. Xue, F. Foret, Y. M. Dunayevskiy, P. M. Zavracky, N. E. McGruer and B. L. Karger, *Anal. Chem.*, 1997, **69**(3), 426–430.
- 11 W. W. Deng, J. F. Klemic, X. H. Li, M. A. Reed and A. Gomez, *J. Aerosol Sci.*, 2006, **37**(6), 696–714.
- 12 R. T. Kelly, J. S. Page, Q. Z. Luo, R. J. Moore, D. J. Orton, K. Q. Tang and R. D. Smith, *Anal. Chem.*, 2006, **78**(22), 7796–7801.
- 13 T. Koerner, K. Turck, L. Brown and R. D. Oleschuk, *Anal. Chem.*, 2004, **76**(21), 6456–6460.
- 14 G. T. T. Gibson, R. D. Wright and R. D. Oleschuk, *Mass Spectrom.*, 2011, in press.
- 15 R. T. Kelly, J. S. Page, I. Marginean, K. Q. Tang and R. D. Smith, *Anal. Chem.*, 2008, **80**(14), 5660–5665.
- 16 R. T. Kelly, J. S. Page, K. Q. Tang and R. D. Smith, *Anal. Chem.*, 2007, **79**(11), 4192–4198.
- 17 R. T. Kelly, J. S. Page, R. Zhao, W. J. Qian, H. M. Mottaz, K. Q. Tang and R. D. Smith, *Anal. Chem.*, 2008, **80**(1), 143–149.
- 18 Q. Luo, J. S. Page, K. Q. Tang and R. D. Smith, *Anal. Chem.*, 2007, **79**(2), 540–545.
- 19 T. Nissila, L. Sainiemi, T. Sikanen, T. Kotiaho, S. Franssila, R. Kostiaainen and R. A. Ketola, *Rapid Commun. Mass Spectrom.*, 2007, **21**(22), 3677–3682.
- 20 L. Sainiemi, T. Nissila, V. Jokinen, T. Sikanen, T. Kotiaho, R. Kostiaainen, R. A. Ketola and S. Franssila, *Sens. Actuators, B*, 2008, **132**(2), 380–387.
- 21 I. Hayati, A. Bailey and T. F. Tadros, *J. Colloid Interface Sci.*, 1987, **117**(1), 222–230.
- 22 R. P. A. Hartman, J. P. Borra, D. J. Brunner, J. C. M. Marijnissen and B. Scarlett, *J. Electrostat.*, 1999, **47**(3), 143–170.
- 23 R. P. A. Hartman, D. J. Brunner, D. M. A. Camelot, J. C. M. Marijnissen and B. Scarlett, *J. Aerosol Sci.*, 1999, **30**(7), 823–849.
- 24 S. S. Yoon, S. D. Heister, J. T. Epperson and P. E. Sojka, *J. Electrostat.*, 2001, **50**(2), 91–108.
- 25 C. B. J. Alejandro, Numerical Simulation of a Single Emitter Colloid Thruster in Pure Droplet Cone-Jet Mode, Ph. D. thesis, Massachusetts Institute of Technology, 2005.
- 26 <http://www.ansys.com/>.
- 27 <http://www.flow3d.com/>.
- 28 J. Zeng, D. Sobek and T. Korsmeyer, *Boston Transducers'03: Digest of Technical Papers*, vol. 1 and 2, 2003, pp. 1275–1278.
- 29 D. A. Saville, *Annu. Rev. Fluid Mech.*, 1997, **29**, 27–64.
- 30 O. Lastow and W. Balachandran, *J. Electrostat.*, 2006, **64**(12), 850–859.
- 31 A. K. Sen, J. Darabi and D. R. Knapp, *Microfluid. Nanofluid.*, 2007, **3**(3), 283–298.
- 32 J. R. Melcher and G. I. Taylor, *Annu. Rev. Fluid Mech.*, 1969, **1**, 111–146.
- 33 R. L. Grimm and J. L. Beauchamp, *J. Phys. Chem. A*, 2010, **114**(3), 1411–1419.
- 34 L. Konermann, *J. Am. Soc. Mass Spectrom.*, 2009, **20**(3), 496–506.
- 35 K. Tang and R. D. Smith, *J. Am. Soc. Mass Spectrom.*, 2001, **12**(3), 343–347.
- 36 J. R. Melcher, *Continuum Electromechanics*, MIT Press, Cambridge, Mass, 1981.
- 37 C. W. Hirt and B. D. Nichols, *J. Comput. Phys.*, 1981, **39**(1), 201–225.
- 38 A. K. Sen, J. Darabi, D. R. Knapp and J. Liu, *J. Micromech. Microeng.*, 2006, **16**(3), 620–630.
- 39 I. Marginean, R. D. Smith, R. T. Kelly, D. C. Prior, B. L. LaMarche and K. Q. Tang, *Anal. Chem.*, 2008, **80**(17), 6573–6579.
- 40 I. Marginean, R. T. Kelly, J. S. Page, K. Q. Tang and R. D. Smith, *Anal. Chem.*, 2007, **79**(21), 8030–8036.
- 41 P. Nemes, I. Marginean and A. Vertes, *Anal. Chem.*, 2007, **79**(8), 3105–3116.
- 42 J. F. de la Mora and I. G. Loscertales, *J. Fluid Mech.*, 1994, **260**, 155–184.
- 43 A. M. Ganan-Calvo, *Phys. Rev. Lett.*, 1997, **79**(2), 217–220.
- 44 S. Q. Su, G. T. T. Gibson, S. M. Mugo, D. M. Marecak and R. D. Oleschuk, *Anal. Chem.*, 2009, **81**(17), 7281–7287.
- 45 R. Bocanegra, D. Galan, M. Marquez, I. G. Loscertales and A. Barrero, *J. Aerosol Sci.*, 2005, **36**(12), 1387–1399.